Bimodal Distribution of Gold in Pyrite and Arsenopyrite: Examples from the Archean Boorara and Bardoc Shear Systems, Yilgarn Craton, Western Australia

Anthony A. Morey,

predictive mineral discovery*Cooperative Research Centre, School of Geosciences, Monash University, Clayton, Victoria 3800, Australia

Andrew G. Tomkins,[†]

School of Geosciences, P.O. Box 28E, Monash University, Clayton, Victoria 3800, Australia

Frank P. Bierlein,

*Centre for Exploration Targeting and Tectonics Special Research Centre, School of Earth and Geographical Sciences,
University of Western Australia, Crawley, Western Australia 6009, Australia*

Roberto F. Weinberg,

School of Geosciences, Monash University, Clayton, Victoria 3800, Australia

and Garry J. Davidson

ARC Centre of Excellence in Ore Deposits, School of Earth Sciences, University of Tasmania, Hobart, Tasmania 7001, Australia

Abstract

This study investigates the microstructures, geochemistry, and hydrothermal evolution of gold-bearing pyrite and arsenopyrite from six orogenic gold deposits in the Archean Eastern Goldfields Province, Western Australia. Scanning electron microscope (SEM), electron microprobe (EMP) and laser ablation-inductively coupled plasma-mass spectroscopy (LA-ICP-MS) analyses show that the gold-bearing minerals possess a number of similar textural features, including the occurrence of invisible gold within initial phases of growth, and later-stage visible gold associated with alteration rims. The alteration rims are characterized by a higher-than-average atomic mass (mainly owing to arsenic enrichment) and are preferentially located along fractures and grain boundaries in the pyrite and arsenopyrite. These observations suggest that visible gold formation is associated with hydrothermal alteration of preexisting pyrite and arsenopyrite. Textural observations and LA-ICP-MS data suggest that some invisible gold was remobilized from early-formed pyrite and arsenopyrite to form visible gold during development of these alteration rims. Gold may also have been added by hydrothermal fluids during a later stage of mineralization. In situ geochemistry and phase relationships of alteration rims are used to further constrain the hydrothermal process responsible for formation of alteration rims and visible gold in fractures. Based on sulfide stability relations, our data indicate that development of arsenopyrite alteration rims associated with late-stage visible gold formation was related to an increase in temperature (maximum increase from 310º to 415ºC) and up to of sic orders of magnitude increase in sulfur fugacity, whereas changes in oxygen fugacity were less important. LA-ICP-MS analyses show that the relative and absolute variations in selected trace element (Au, Ag, Sb, Bi, Ba, Te, Pb, Co, and Mo) concentrations can also be used to distinguish between unaltered and altered pyrite and arsenopyrite. In general, trace elements within pyrite and arsenopyrite have a relatively uniform distribution, whereas later-stage alteration rims have more variable trace element distributions. Although the observed textures are typical of prograde metamorphic coronae, we suggest that they are the consequence of variations in fluid conditions and chemistry, and that mineralization occurred in response to syn- and/or postpeak metamorphic fluid infiltration.

Introduction

Gold is commonly associated with sulfide and sulfarsenide minerals within many hypogene ore systems, including sediment-hosted disseminated gold, or Carlin-type (e.g., Bakken et al., 1989; Arehart et al., 1993; Palenik et al., 2004), orogenic (e.g., Mumin et al., 1994; Genkin et al., 1998; Ashley et al., 2000), epithermal (e.g., Griffin et al., 1991) and intrusion-related systems (e.g., Lang and Baker, 2001; Marsh et al., 2003). Past studies have assessed the nature, chemical state, and distribution of gold relative to these sulfarsenides (see Cabri et al., 2000, for a review). However, the physiochemical controls on gold mineralization are still emerging, with fluid temperature, pH, and oxidation or sulfidation state all playing important roles (e.g., Heinrich and Eadington, 1986; Cathelineau et al., 1989; Mikucki and Ridley, 1993).

The concentration and distribution of gold in sulfide and sulfarsenide phases vary considerably, ranging from tens of ppb to more than 1 wt percent (Cabri et al., 1989, 1998; Cathelineau et al., 1989) and occurring as invisible or visible phases that were deposited or remobilized by multistage hydrothermal or metamorphic events (e.g., Neumayr et al., 1993; Oberthür et al., 1997; Genkin et al., 1998; Tomkins and Mavrogenes, 2001). Invisible gold can occur in solid solution within the host crystal lattice or exist as <1 μm, submicroscopic particles

---

[†] Corresponding author: e-mail, andy.tomkins@sci.monash.edu.au

(Cabri et al., 1989; Genkin et al., 1998; Palenik et al., 2004). The chemical state of gold in solid solution is complex, with studies suggesting an oxidation state of Au^{3+} (e.g., Arehart et al., 1993) or a combination of Au^0 and Au^{1+} (e.g., Simon et al., 1999). Arsenopyrite grains also can host Au^0 and Au^{1+} (Cabri et al., 2000). A number of studies show that Au in solid solution exchanges for Fe sites within arsenopyrite and pyrite (Wu and Delbove, 1989; Fleet and Mumin, 1997; Tarnocai et al., 1997). Oscillatory-zoned arsenic-rich growth bands in pyrite also typically correlate with elevated gold concentrations (e.g., Fleet et al., 1989; Fleet and Mumin, 1997), where growth bands enriched in As and depleted in Fe carry higher concentrations of gold (Genkin et al., 1998; Johan et al., 1989). In orogenic systems, gold commonly has a bimodal distribution in which invisible gold within arsenopyrite is overprinted by later visible gold (Coleman, 1957; Mumin et al.,

1994; Oberthür et al., 1997; Genkin et al., 1998). This study examines the textures, mineralogy, and overprinting relationships of composite gold-bearing pyrite and arsenopyrite grains to further define their characteristics. Moreover, by using multiple microbeam analytical techniques and phase stability diagrams to understand the different major- and trace-element compositions of arsenopyrite, we further constrain processes associated with the formation of this common ore type.

Geologic Setting

Samples of gold mineralization were collected from the Boorara shear zone and the Bardoc tectonic zone, which are broad (>5 km wide in map view), crustal-scale shear systems within the Eastern Goldfields Province of the Archean Yilgarn craton (Witt, 1993; Swager, 1997; Fig. 1). The Eastern
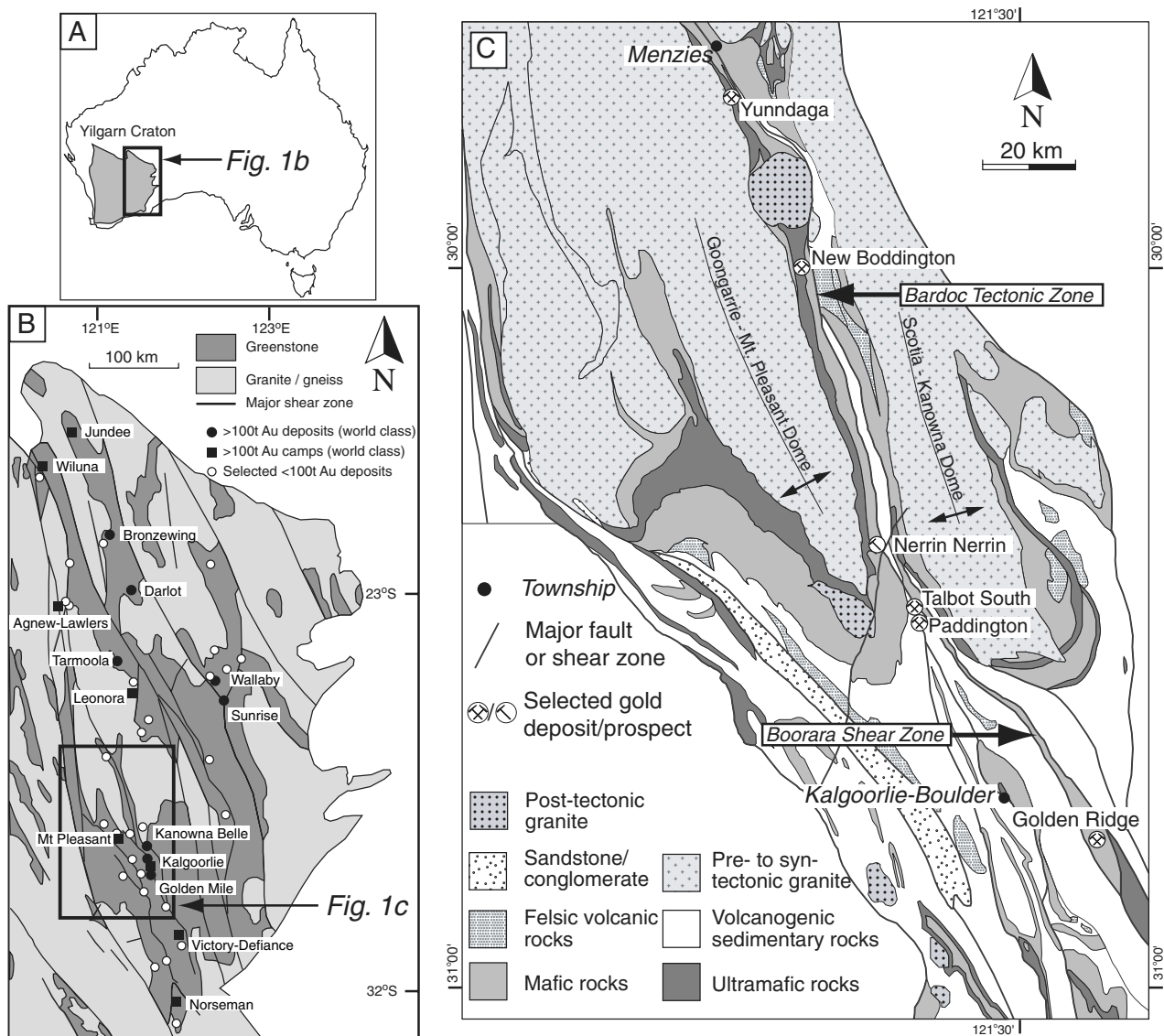

FIG. 1. Regional geology and study locations. A) Location of the Archean Yilgarn craton. B) Eastern Goldfields Province, showing major shear systems and gold deposits. C) Geology map of part of the Eastern Goldfields Province, showing the distribution of supracrustal units, granitoids, major shear systems and localities related to this study. Modified after Hagemann and Cassidy (2000), Swager and Griffin (1990).

Goldfields Province hosts a number of world-class gold deposits that are distributed along major fault systems and their subordinate structures (e.g., Groves et al., 1984; Eisenlohr et al., 1989; Fig. 1B). This region has a geologic history spanning ca. 2710 to 2600 Ma (e.g., Swager, 1997), beginning with the formation of mafic, ultramafic, and volcanogenic sedimentary rock sequences and followed by multiple stages of ductile-brittle deformation, metamorphism, and widespread granitic intrusion (Champion and Sheraton, 1997; Swager, 1997). This deformation produced the major north-northwest–trending shear systems preserved today, and orogenic gold mineralization occurred late within the tectonothermal history of the Eastern Goldfields Province, generally constrained between ca. 2655 and 2625 Ma (Groves et al., 2000; Brown et al., 2002; Salier et al., 2005).

Mineralized samples were selected from one gold deposit within the Boorara shear zone (Golden Ridge, Fig. 1C) and from four deposits and one prospect within Bardoc tectonic zone (Paddington Talbot South, Nerring Nerrin, New Boddington, and Yunndaga). All mineralized rocks from the Bardoc tectonic zone are hosted within mafic extrusive or intrusive units, whereas the host unit for the Golden Ridge deposit is a felsic porphyry. All samples studied were taken from arsenopyrite- and/or pyrite-rich wall-rock alteration halos directly adjacent to quartz-carbonate veins, as this is where the highest gold grades occur. The predominance of wall-rock–hosted gold indicates that the ore formation was a product of wall-rock reaction rather than precipitation in veins, a feature that is typical of orogenic deposits within the Eastern Goldfields Province (e.g., Mikucki, 1998). A summary the characteristics of the gold deposits is given in Table 1.

The Golden Ridge deposit is the largest known gold mine within the Boorara shear zone (Fig. 1C), with a production of approximately 8 t of gold from 1904 to 2003. Gold mineralization dominantly occurs in hydrothermally altered rocks adjacent to planar quartz-carbonate-plagioclase veins that are generally <1 m thick and hosted within an intensely veined and altered felsic porphyry unit (Fig. 2A). Within 1 m of the vein margin, wall-rock alteration is characterized by quartz, carbonate, muscovite, chlorite, anorthite, sulfide, and ilmenite. The sulfur-bearing phases are dominated by arsenopyrite, followed by pyrite, sphalerite, and chalcopyrite.

Analytical Methods

Optical and SEM imagery were used to define ore textures, and EMP and LA-ICP-MS were used for the qualitative and quantitative characterization of gold-bearing pyrite and arsenopyrite grains. A Jeol™ JSM 6300 SEM at the University of Ballarat was used, with a 15 kV and 1.5 nA electron beam. Backscattered electron images (BSE) and energy dispersive X-ray spectroscopy (EDS) data were acquired using an Oxford Instruments four element quadrant detector. The EMP data were acquired using a Cameca SX50 Electron Microprobe with four vertical wavelength dispersive spectrometers at the School of Earth Sciences, University of Melbourne. The accelerating voltage for the EMP was 15 kV with a beam current of 35 or 25 nA. Elements analyzed were S, Fe, As, Sb, Te, and W. For these elements, the counting time was 20 s and the average detection limit is 0.06 at. percent.

A New Wave OP213 laser probe and HP4500 quadrupole ICP-MS from the Centre of Ore Deposit Research, University of Tasmania, Hobart, was used for major and trace element analysis of gold-bearing pyrite and arsenopyrite. This LA-ICP-MS was used for both quantitative spot (Table 2; Fig. 2) and qualitative line scan analyses. Qualitative analyses consisted of a 30 s background run and a 60 s analysis time, with data only above detection limits presented. The precision and detection limits for the quantitative spot analyses are shown in Table 2. Ablation spot sizes were 30 μm at a frequency of 10 Hertz and ~6.5 J/cm². Calibration techniques for the spot analyses follow Norman et al. (2003) and Danyushevsky et al. (2003, 2004), using standard reference material (STDGL2b-2). Iron concentrations in an internal standard were determined through EMP analyses. There is currently no widely available standard reference material suitable for the analyses of trace elements within sulfide minerals using the LA-ICP-MS (e.g., Sylvester

TABLE 1. Major Characteristics of Each Deposit/Study Locality

Deposits from south to north	Gold mined (t Au)	Host lithology	Metamorphic facies	Vein structure	Alteration assemblage[1] (in decreasing abundance)
Paddington laminated vein	40	Dolerite and basalt	Greenschist	Shear vein	Carb, qtz, ms, bt, apy, other sulfides, Fe oxides
Paddington ladder vein		Dolerite and basalt	Greenschist	Planar vein	Carb, qtz, ms, apy, other sulfides, Fe oxides
Talbot South	12	Gabbro	Greenschist	Brecciated and planar veins	Qtz, carb, ms, chl, ± bt, apy, other sulfides, Fe oxides
Nerrin Nerrin	0.02	Dolerite	Greenschist	Planar veinlets	Qtz, carb, ms, chl, apy, other sulfides, Fe oxides
New Boddington	<1	Basalt	Greenschist	Stockwork and planar veins	Carb, qtz, chl, bt, ms, apy, other sulfides, Fe oxides
Yunndaga	8	Contact between sedimentary rock and dolerite	Lower amphibolite	Shear laminated vein	Qtz, carb, bt, ms, apy, other sulfides, Fe oxides
Golden Ridge	8	Felsic porphyry	Greenschist	Conjugate planar veins	Qtz, carb, ms, chl, apy, py

[1] Abbreviations : apy = arsenopyrite, bt = biotite, carb = carbonate, chl = chlorite, ms = muscovite, qtz = quartz
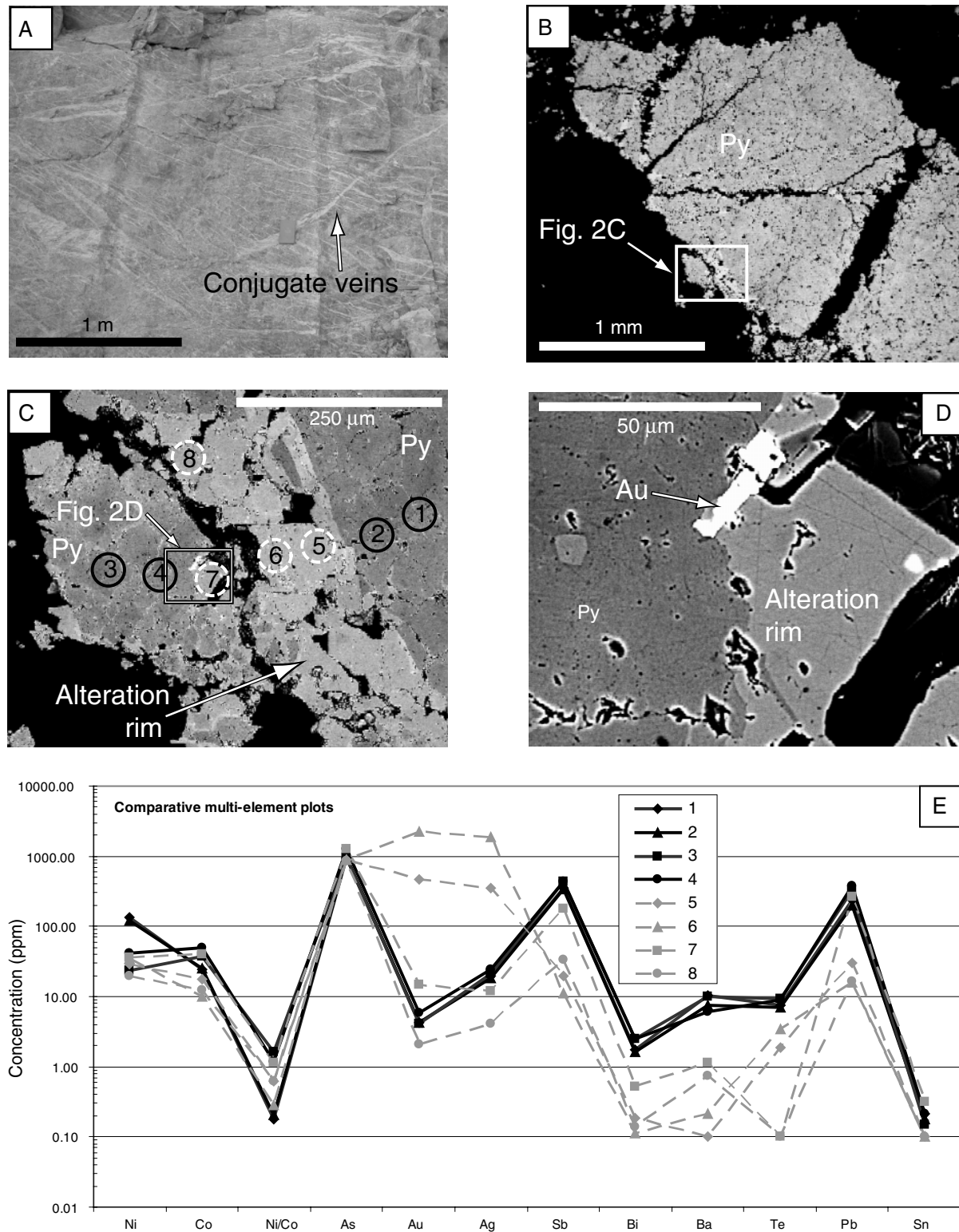
FIG. 2. Images and geochemistry of pyrite (Py)-dominated ore from the Golden Ridge deposit. A) View of the pit wall showing mineralized planar conjugate veins hosted within a felsic porphyry unit. B) Backscattered electron image of a pyrite grain showing well-developed fractures and erratic grain boundaries, indicating significant postcrystallization alteration. C) Close-up backscattered electron image of the pyrite grain margin showing a fracture plane (black) and adjacent alteration rim. Also shown are laser ablation analysis numbers from unaltered (solid lines) and altered (dashed lines) pyrite (refer to Table 2). D) Close up of C, showing a visible gold grain within the altered part of an alteration rim boundary. E) LA-ICP-MS absolute data for As and trace elements of unaltered (solid lines) and altered (dashed lines) pyrite from positions referred to in image C. Refer to Table 2 for data used within the plot.

TABLE 2. LA-ICP-MS Data of Pyrite from Golden Ridge (ppm; see Fig. 2C, E)

Analysis no.	Ni	Co	Ni/Co	As	Au	Ag	Sb	Bi	Ba	Te	Pb	Sn
Average detection limit	0.20	0.64	-	5.0	0.076	0.21	0.15	0.025	0.12	1.22	0.073	0.11
Precision (%)	5.05	5.6	-	3.57	14	12	6.2	11	15	18	6.5	11
1	132.24	24.06	0.18	938.96	4.25	19.39	350.95	1.77	10.28	7.55	238.49	0.22
2	120.64	24.94	0.21	991.45	4.27	18.22	335.56	1.63	7.43	7.08	201.83	0.18
3	23.13	37.84	1.64	938.69	4.13	21.18	431.19	2.50	9.92	9.25	322.78	0.15
4	42.19	49.12	1.16	1274.03	5.94	24.47	430.99	2.46	6.12	8.86	379.45	0.21
5	28.64	17.96	0.63	902.59	460	346	19.62	0.19	<0.12	1.86	29.77	<0.11
6	34.37	9.83	0.29	873.92	2277	1856	11.30	0.11	0.21	3.45	15.65	<0.11
7	36.25	40.59	1.12	1282.10	14.75	11.89	182.07	0.52	1.16	<1.22	262.97	0.32
8	19.80	12.23	0.62	866.54	2.09	4.13	33.40	0.14	0.74	<1.22	16.19	<0.11

et al., 2005). This study focuses on the relative changes in major and trace elements within arsenopyrite and pyrite and not their absolute values. For the STDGL2b-2 reference material, the standard deviation for most elements is <6 percent and platinum group elements and Au have a standard deviation of ~15 percent (Danyushevsky et al., 2003). For qualitative LA-ICP-MS line scans, the line width was 25 μm, the frequency 10 Hertz and total analysis times ranged from 2.5 to 3.5 minutes.

Results from SEM, EMP, and LA-ICP-MS Analyses

Gold in pyrite

The samples from Golden Ridge are dominated by pyrite and were collected from diamond drill core intersections (~5 ppm Au) in wall rock adjacent to quartz-carbonate veins (Fig. 2B). The gold-bearing pyrite grains (Fig. 2B) are pervasively fractured, have irregular grain boundaries, and BSE images show that the bulk of the pyrite grains are relatively uniform in composition. Parallel to the fractures and grain boundaries, however, narrow composite rims within pyrite are characterized by a higher than average atomic mass (Fig. 2C-E). These rims vary in their dimensions but are in general up to 250 μm in thickness from grain boundaries and fracture margins. As shown in Figure 2C and D, the rims define zones where selective chemical modification of the preexisting pyrite parallel to fracture-grain boundaries has taken place. This grain boundary-fracture association suggests an external influence, and given the lack of other mineral phases containing As and S, introduction of a late hydrothermal fluid is thought to be responsible. This fluid would have penetrated along grain boundaries, possibly promoting fracturing and facilitating reaction progress. The resulting pyrite rims are thus considered to be alteration rims. Visible gold grains are only observed within these alteration rims, and along margins between altered and unaltered pyrite (Fig. 2D, E).

Electron microprobe data indicate that As concentrations are less than 1 at percent in unaltered pyrite (Table 3), and altered rims are marginally enriched in As by approximately 0.01 at percent. These low As contents are typical of pyrite in Yilgarn gold deposits (Dahl et al., 1987). Sulfur concentrations within rims are enriched, and Fe concentrations are depleted by ~0.1 at percent. Trace elements in unaltered pyrite (e.g., Sb, Te, W) also do not vary significantly, with relatively less Sb and Te in the altered rims and negligible variation in W (Table 3).

In contrast to the EMP data, the LA-ICP-MS results (Fig. 2D, E; Table 2) highlight systematic variations between unaltered bulk pyrite and altered rims, particularly for Au, Ag, Sb, Bi, Ba, Te, Pb, and Sn. The LA-ICP-MS data also show that As concentrations do not vary significantly between unaltered pyrite and alteration rims, invisible Au and Ag (up to 5.94 and 24.47 ppm, respectively; Table 2) exist within the unaltered pyrite, and concentrations of trace elements within the unaltered pyrite domains are more uniform than in the alteration rims. Elevated (<2,277 ppm), albeit highly variable, Au and Ag concentrations within the alteration rims contribute to their increased average atomic mass as determined by BSE images (Fig. 2C, D). All other trace elements are less abundant in the pyrite alteration rims.

Gold in arsenopyrite

Gold in arsenopyrite was examined in samples from the Paddington, Talbot South, New Boddington, and Yunndaga gold deposits and the Nerrin Nerrin gold prospect (Fig. 1C; Table 1). All samples are hosted within mafic rocks adjacent to brittle-ductile quartz-carbonate veins. Wall-rock alteration

TABLE 3. Electron Microprobe Data of Gold-Bearing Pyrite from Golden Ridge, Comparing Primary Growth Zones with Alteration Rims (values in at %)

Analysis no.	Details	Fe	S	As	Sb	Te	W	Total
10380-b	Primary zone	33.83	66.07	0.077	–	–	–	100
10380-c	Primary zone	33.57	66.32	0.088	–	–	–	99.9
10380-f	Primary zone	33.71	66.17	0.082	–	–	–	100
10380-a	Alteration rim	33.55	66.34	0.099	–	–	–	99.9
10380-d	Alteration rim	33.60	66.30	0.098	–	–	–	99.9
10380-e	Alteration rim	33.37	66.55	0.11	–	–	–	100

– = below detection limit; analytical detection limit for all elements is 0.06 at percent

in these deposits is characterized by carbonate, quartz, muscovite, chlorite ± biotite, and opaque alteration phases (arsenopyrite, with lesser pyrite, pyrrhotite, sphalerite, chalcopyrite ± ilmenite ± rutile) and visible gold. Examples of representative vein styles and microstructures from these

Bardoc tectonic zone localities are shown in Figure 3A to F. At all localities, the overprinting relationships of the opaque phases define a uniform three-stage alteration history: stage 1 pyrrhotite grains were overprinted by stage 2 arsenopyrite, which is in turn overprinted by stage 3 arsenopyrite rims,
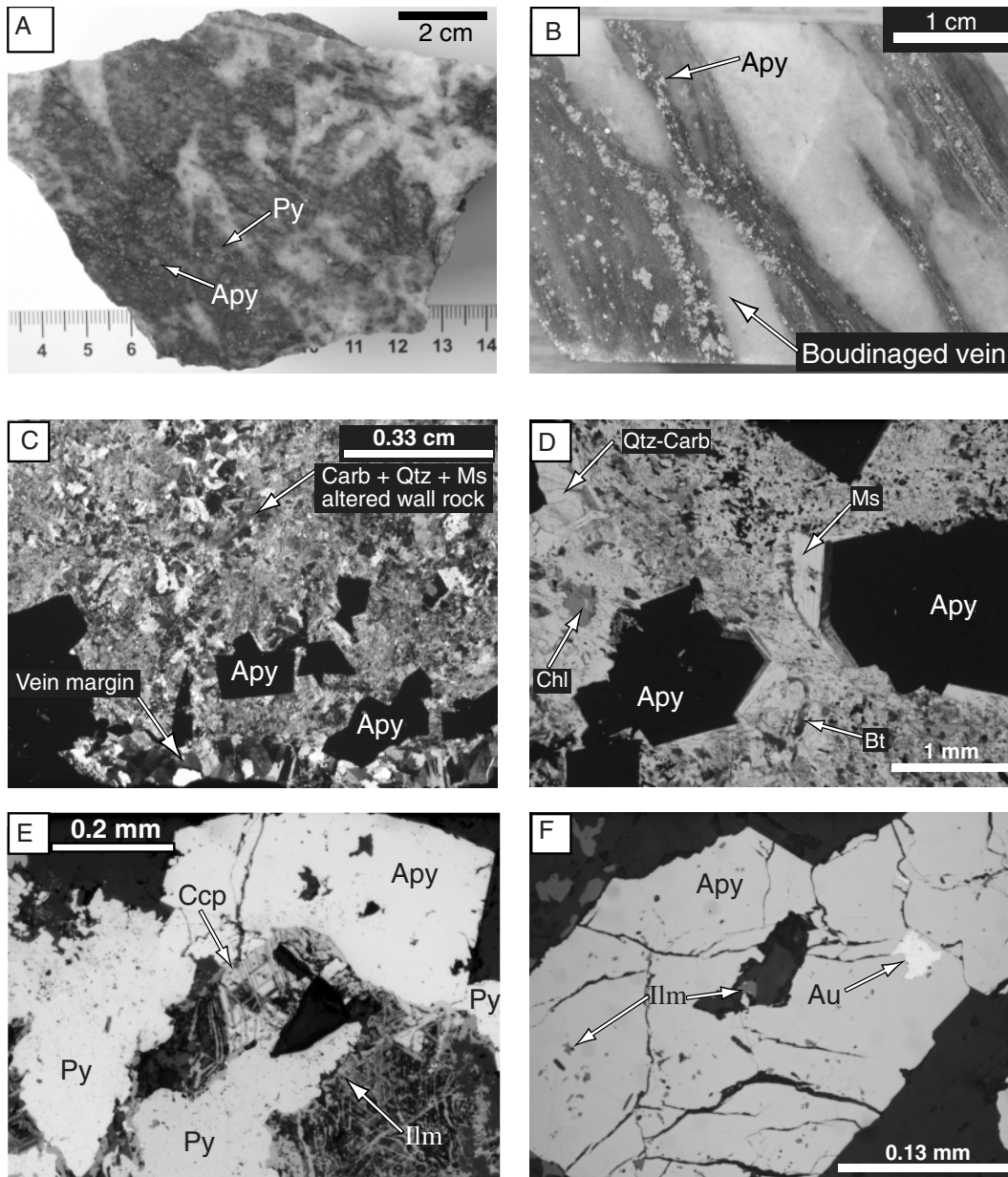

FIG. 3. Representative images of arsenopyrite-dominated ore samples from the Bardoc tectonic zone. A) Brecciated gabbro from the Talbot South deposit, showing quartz-carbonate vein infill and arsenopyrite- and pyrite-bearing wall-rock fragments. B) Ductile laminated vein from the Yunndaga deposit, showing boudinaged quartz-carbonate veins hosted within arsenopyrite-dominated alteration wall-rock selvages. C) Transmitted light photomicrograph of a wall-rock alteration assemblage adjacent to a ladder vein, Paddington deposit. Shown are carbonate, quartz, muscovite and opaque arsenopyrite alteration minerals. Cross-polarized light. D) Transmitted light photomicrograph of a wall-rock alteration assemblage from the New Boddington deposit; similar to C; however, biotite and chlorite are also present within the alteration assemblage. Plane-polarized light. E) Photomicrograph from the Talbot South deposit showing overprinting relationships of opaque minerals within the mineralized alteration assemblage. Arsenopyrite has been hydrothermally embayed and consequently overprinted by pyrite, chalcopyrite, and ilmenite. F) Reflected light photomicrograph of a gold-bearing arsenopyrite grain from New Boddington, showing visible gold associated with fractures and ilmenite filling cavities within arsenopyrite. Apy = arsenopyrite, Bt = biotite, Carb = carbonate, Ccp = chalcopyrite, Chl = chlorite, Ilm = ilmenite, Ms = muscovite, Py = pyrite, Qtz = quartz.

pyrite, base metal sulfides, ilmenite, and visible gold grains (summarized in Fig. 4, with textural evidence provided in Fig. 3E, F). This consistent, three-stage alteration history is found over a strike length of 80 km, suggesting that close to uniform mineralization conditions occurred throughout the whole Bardoc tectonic zone (Morey et al., 2007b).

BSE images reveal that gold-bearing arsenopyrite grains also have intragranular compositional zones related to a dynamic alteration history. The arsenopyrite grains are products of hydrothermal alteration showing, in some cases, primary crystallographic zoning (e.g., Fig. 5A-C), with fracture margins, grain boundaries, and intragrain domains also characterized

Locality	Overprinting relationships of opaque phases		
	Stage 1	Stage 2	Stage 3
Yunndaga	Po $\longrightarrow$	Apy + Au $\longrightarrow$	Po + Py + Sp + Au + Ccp
New Boddington	Po $\longrightarrow$	Apy + Py + Au $\longrightarrow$	Po + Ccp + Ilm + Au
Nerrin Nerrin	Po $\longrightarrow$	Apy + Au $\longrightarrow$	Py + Ilm + Au
Talbot South	Po $\longrightarrow$	Apy + Au $\longrightarrow$	Py + Ccp + Rt + Au
Paddington *Laminated* and *ladder* veins	Po $\longrightarrow$	Apy + Au $\longrightarrow$	Py + Ccp + Gn + Rt + Au

FIG. 4. Diagram showing the overprinting relationships of opaque phases from the Bardoc tectonic zone. Gold in stage 2 is invisible, whereas Au in stage 3 is visible. Apy = arsenopyrite, Au = visible/invisible gold, Ccp = chalcopyrite, Gn = garnet, Ilm = ilmenite, Po = pyrrhotite, Py = pyrite, Rt = rutile, Sp = sphalerite.
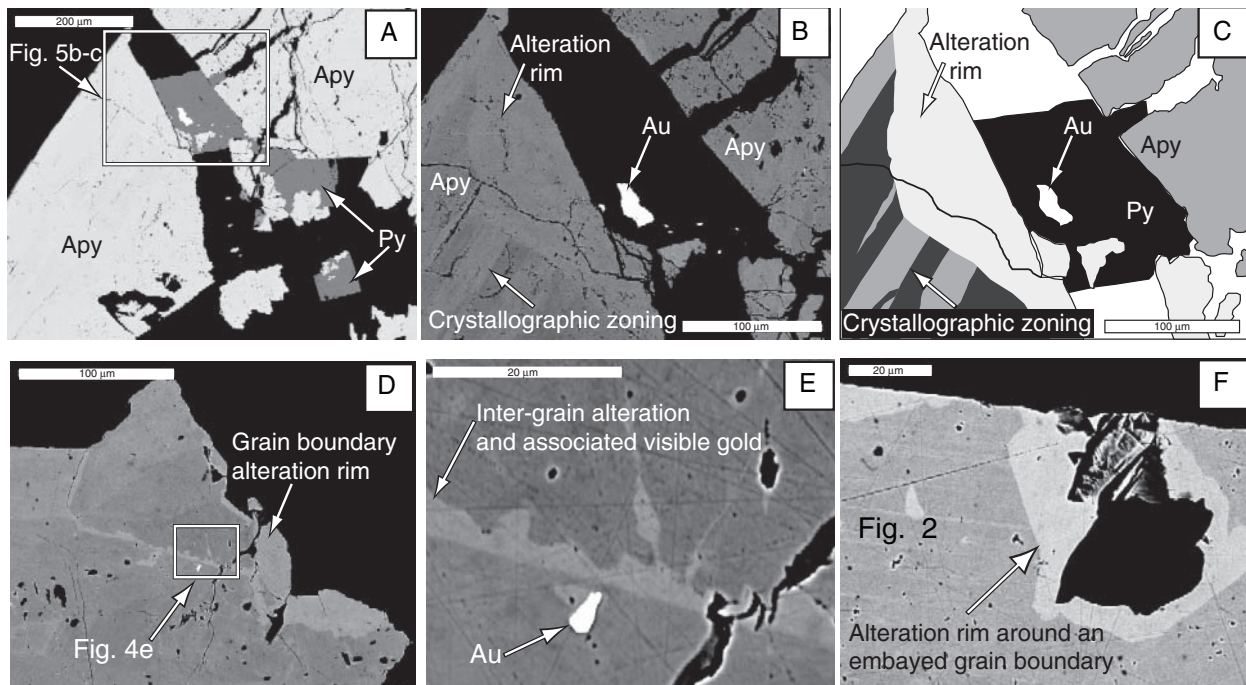

FIG. 5. Collection of backscattered electron images defining the characteristics of alteration rims within gold-bearing arsenopyrite, Bardoc tectonic zone. A) Laminated vein sample from the Paddington deposit showing fractured arsenopyrite infilled with later-stage pyrite. B) Close-up of A, with contrast adjusted to show a visible gold inclusion within the fracture-filling pyrite grain and crystallographic zoning within arsenopyrite being truncated by and alteration rim. C) Schematic representation of image in B highlighting the alteration rim. D) Arsenopyrite from the New Boddington deposit, showing both intergrain and grain boundary alteration rims. E) Close-up of image D, showing the association later-stage between alteration rims and visible gold. F) Close-up of an arsenopyrite grain from the Yunndaga deposit showing small-scale dissolution of a grain boundary and subsequent alteration of the substrate. Apy = arsenopyrite, Py = pyrite.

by higher average atomic mass rims or zones (Fig. 5B-F). As noted above, the observation that these enriched zones occur adjacent to fractures and grain boundaries suggests that they most likely represent a hydrothermal alteration event that took place during fracturing of arsenopyrite. As in the pyrite-dominated ore from Golden Ridge, the formation of visible gold (Fig. 5A-E) is thought to be related to this fracturing and alteration. Pyrite, base metal sulfides, Fe oxides, ± pyrrhotite are also associated with this later-stage hydrothermal event (Figs. 3E-F, 5A). The visible gold grains occur as inclusions within stage 3 pyrite, as solitary grains in fractures and at grain boundaries in arsenopyrite or within stage 3 arsenopyrite alteration rims (Fig. 5).

The EMP analyses (Tables 4, 5) show that unaltered and altered arsenopyrite grains from the Bardoc tectonic zone have As concentrations that range between 28.9 and 33.2 at percent, with corresponding variations in S content (33.3–37.4 at

% S; pyrite analyses in Table 6). Concentrations of Fe, however, remain relatively uniform (33.5 to 34.0 at %). As has been noted in experimental studies (Kretschmar and Scott, 1976; Sharp et al., 1985), this antithetic correlation suggests that As and S represents a coupled substitution within arsenopyrite in response to changing conditions. Alteration rims on arsenopyrite are characterized by higher average atomic mass (Fig. 5B-F) with, on average, 1.5 at percent more As and 1.5 at percent less S (Tables 4 and 5) compared to relatively unaltered arsenopyrite grains. These data indicate that hydrothermal activity associated with alteration rims and visible gold formation enriched the arsenopyrite in arsenic and depleted it in sulfur.

Element maps of arsenopyrite from Yunndaga support the EMP analyses. Alteration rims identified in BSE images (Fig. 6A) are characterized by enrichment in As and depletion in S (Fig. 6B, C), but no detectable variations in Fe are observed within the corresponding Fe element map (Fig. 6D). Other studies have reported that invisible gold in arsenopyrite substitutes either inversely or directly with As (Sb), S, and Fe (Cathelineau et al., 1989; Johan et al., 1989; Wu and Delbove, 1989; Fleet and Mumin, 1997). However, EMP and SEM data on samples from the Bardoc tectonic zone suggest that, in these examples, only As (Sb) and S substitution occurs, and Fe concentrations remain relatively uniform during arsenopyrite alteration.

LA-ICP-MS line scans of arsenopyrite

Quantitative LA-ICP-MS spot analyses on arsenopyrite cores and alteration rims, in contrast to similar analyses on pyrite, did not show any significant differences in trace element concentrations, or the data were erroneous or imprecise. However, qualitative variations in trace elements across composite arsenopyrite zones are apparent in LA-ICP-MS line scans. In arsenopyrite from Nerrin Nerrin, primary crystallographic growth bands (Fig. 7A-B) with relatively low atomic mass coincide with Au peaks, whereas growth bands with relatively high atomic mass correspond with peaks in Bi and Pb. Cobalt and Sb show less consistent variations but suggest a slight decrease in these elements coincident with Au peaks (see point 2, Fig. 7B). It is likely the major elements within arsenopyrite (Fe and As) also vary across each growth zone (Cathelineau et al., 1989), however, this variation is not easily detectable in qualitative LA-ICP-MS traverses.

In an arsenopyrite grain from the New Boddington ore sample (Fig. 7C, D) relatively higher average atomic mass in a zone bordered by a microfracture is interpreted to have undergone postcrystallization hydrothermal alteration. A qualitative line scan across this zone (Fig. 7C, D) indicates concentrations of invisible gold above the detection limit within the primary portion of the arsenopyrite but concentrations below detection within the more altered part of the same grain. From the altered to unaltered arsenopyrite domain, the Ni and Sb traces appear to decrease, whereas the Co trace increases. These observations support quantitative spot analyses, where invisible gold is more abundant within preserved arsenopyrite domains, and visible gold is associated with later-stage overgrowth zones.

An anhedral arsenopyrite grain from the Yunndaga gold deposit (Fig. 7E) also has a higher average atomic mass zone

TABLE 4. Electron Microprobe Data of Initial-Unaltered
Arsenopyrite, Bardoc Tectonic Zone (values in at %)

Analysis no.	Location	Fe	S	As
BW-2	Talbot South	33.8	35.9	30.3
BW-7	Talbot South	33.8	36.5	29.7
S05-f-6	Paddington	34.0	35.2	30.8
S05-g-7	Paddington	33.9	34.6	31.4
S05-h-8	Paddington	33.8	35.8	30.4
S05-l-10	Paddington	33.7	36.3	30.0
S06-k-11	Paddington	33.8	36.5	29.7
S05-l-12	Paddington	33.9	36.8	29.2
S05-o-16	Paddington	33.6	34.8	31.6
GG-1	New Boddington	33.7	37.4	28.9
GG-5	New Boddington	33.9	35.8	30.3
PD-23-6	Paddington	33.7	35.4	30.9
YD-3	Yunndaga	33.7	35.6	30.7
NN-7	Nerrin Nerrin	33.5	36.2	30.2
PD-4	Paddington	33.7	35.1	31.2
	Average	35.9	33.7	30.4
	±2σ	0.232	1.55	1.55

TABLE 5. Electron Microprobe Data of Alteration Rims within
Arsenopyrite, Bardoc Tectonic Zone (values in at %)

Analysis no.	Location	Fe	S	As
BW-3	Talbot South	33.7	35.3	30.9
BW-6	Talbot South	33.6	35.2	31.2
BW-9	Talbot South	33.9	35.2	30.8
BW-10	Talbot South	33.9	34.9	31.2
S05-c-3	Paddington	33.8	34.9	31.2
S05-j-9	Paddington	33.6	33.6	32.8
S05-m-13	Paddington	33.9	33.6	32.4
S05-n-14	Paddington	33.8	34.4	31.8
GG-2	New Boddington	33.8	34.2	31.9
GG-4	New Boddington	33.8	34.2	32.0
PD23-7	Paddington	33.7	34.5	31.8
YD-2	Yunndaga	33.6	33.6	32.7
YD-5	Yunndaga	33.5	33.3	33.2
NN-3	Nerrin Nerrin	33.5	33.5	33.0
NN-6	Nerrin Nerrin	33.7	33.8	32.4
PD-3	Paddington	33.6	34.7	31.7
	Average	33.7	34.3	31.9
	±2σ	0.311	1.34	1.51

TABLE 6. Electron Microprobe Data of Stage 3 Pyrite (syn-visible Au) from the Bardoc Tectonic Zone (at %)

Analysis no.	Location	S	Fe	As	Sb	Te	W	Total
BW-5-1	Talbot South	66.07	33.82	0.084	0.0253	0.0004	0.0003	100.00
BW-8-1	Talbot South	66.44	33.45	0.096	0.0074	0.0004	0.0003	100.00
BW-11-1	Talbot South	66.06	33.72	0.198	0.0067	0.0012	0.0081	100.00
BW-12-1	Talbot South	66.32	33.60	0.067	0.0004	0.0042	0.0057	100.00
BW-13-1	Talbot South	66.38	33.52	0.090	0.0043	0.0004	0.0054	100.00
BW-14-1	Talbot South	65.54	33.82	0.630	0.0013	0.0072	0.0003	100.00
S05-a-1-1	Paddington	66.16	33.57	0.249	0.0004	0.0099	0.0068	100.00
S05-d-4-1	Paddington	65.69	33.85	0.458	0.0004	0.0004	0.0024	100.00
S05-e-5-1	Paddington	65.93	33.49	0.564	0.0080	0.0040	0.0014	100.00
PD23-2-1	Paddington	65.68	33.83	0.491	0.0032	0.0004	0.0003	100.00
PD23-3-1	Paddington	66.27	33.63	0.097	0.0004	0.0004	0.0003	100.00
PD23-4-1	Paddington	66.52	33.38	0.074	0.0004	0.0007	0.0215	100.00
PD23-5-1	Paddington	66.24	33.51	0.247	0.0004	0.0004	0.0071	100.00
PD-1-1	Paddington	66.37	33.41	0.216	0.0004	0.0067	0.0003	100.00
PD-2-1	Paddington	66.00	33.54	0.445	0.0004	0.0004	0.0078	100.00
NN-4-1	Nerrin Nerrin	65.97	33.54	0.460	0.0097	0.0004	0.0189	100.00
NN-5-1	Nerrin Nerrin	66.71	33.24	0.032	0.0004	0.0047	0.0153	100.00
NN-8-1	Nerrin Nerrin	66.25	33.68	0.053	0.0004	0.0015	0.0133	100.00
NN-10-1	Nerrin Nerrin	66.40	33.38	0.217	0.0004	0.0004	0.0003	100.00

within an outer alteration rim. Irregular grain boundaries and pitted crystal surfaces also indicate postcrystallization alteration, with a visible gold grain present near the edge of the grain. A traverse from an overgrowth to primary zone shows systematic variations in the trace element geochemistry. From

the BSE image (Fig. 7E), no visible gold was detected; however, concentrations of invisible gold are consistently above detection limits (~70 counts/s) within the arsenopyrite core (Fig. 7F). The erratic Au signal is most likely due to the low counts per second. Nevertheless, there is a positive correlation
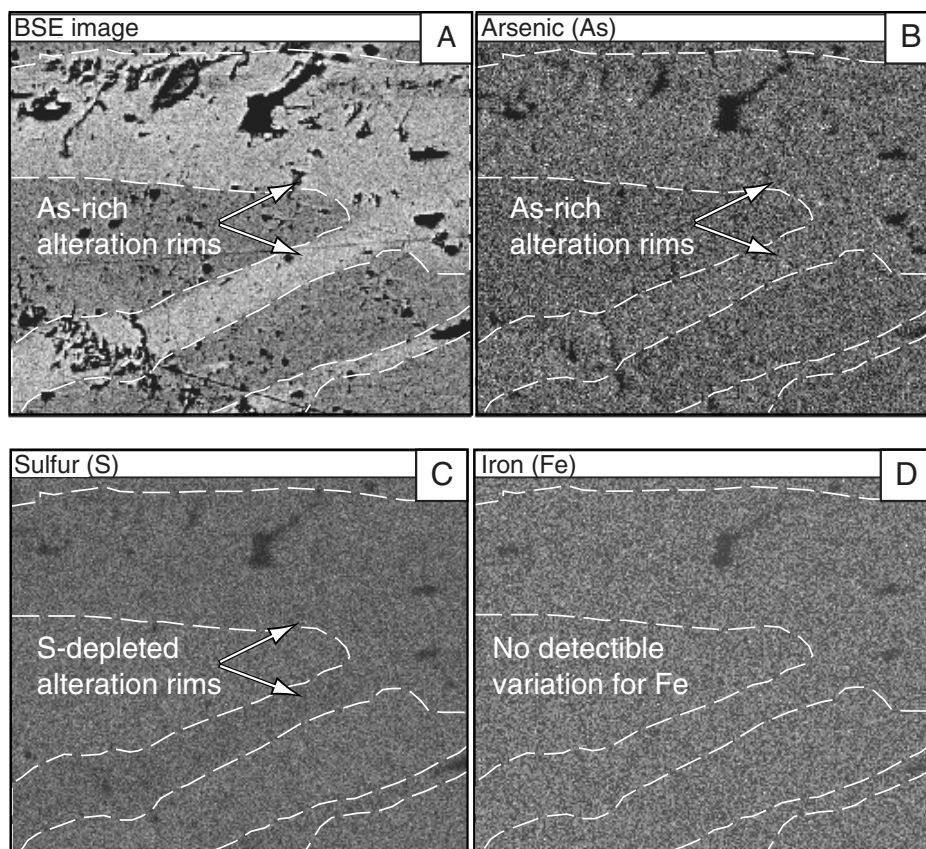

FIG. 6. A) An altered arsenopyrite grain from the Yunndaga deposit showing its relatively higher atomic mass alteration zones (backscattered electron image). B-C) Energy dispersive X-ray spectroscopy (EDS) element maps of the same grain in A, showing subtle contrasts that represent variations in As, S content within arsenopyrite. D) EDS image showing no detectible variation in Fe concentration.
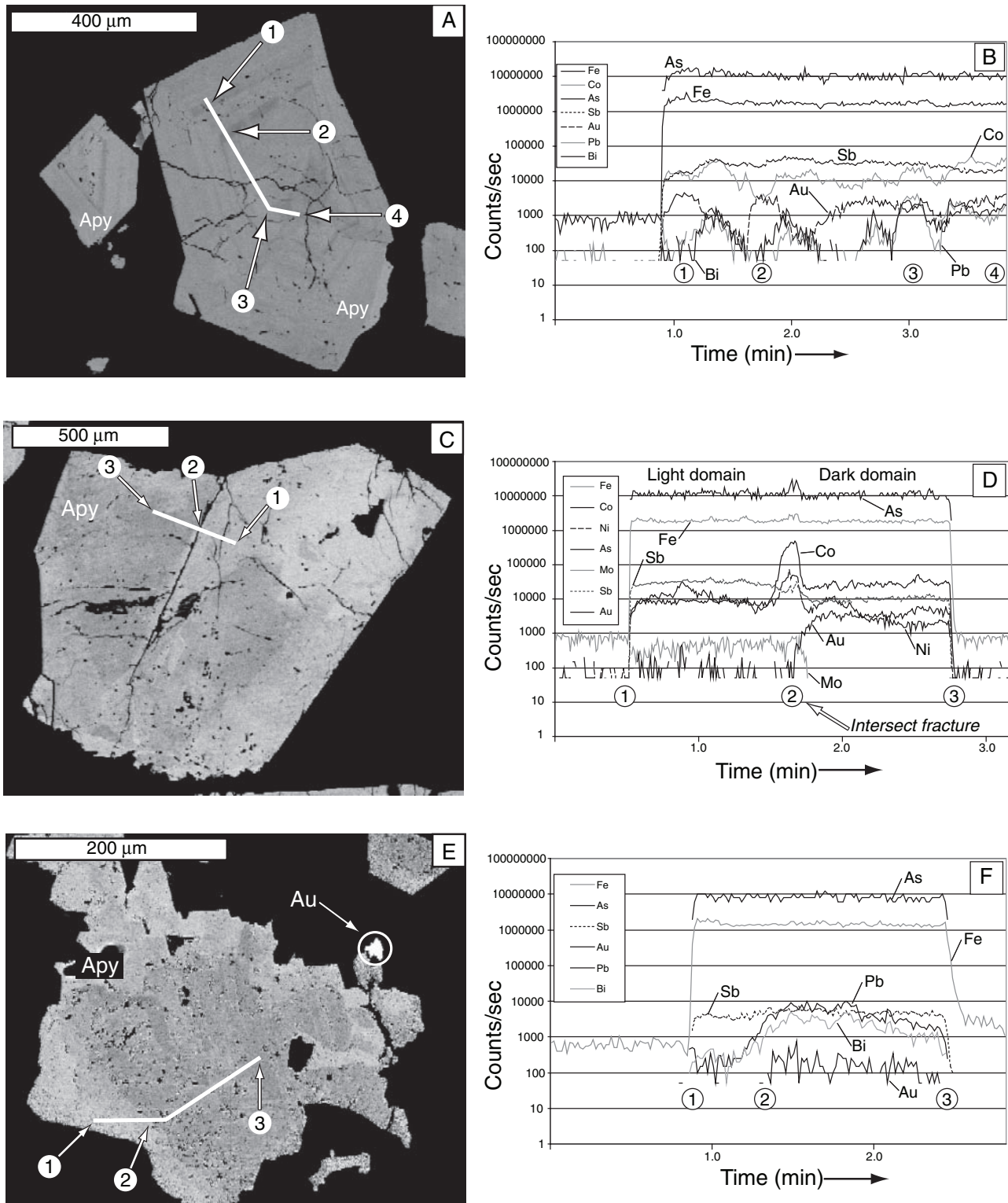
FIG. 7. Details of LA-ICP-MS line analyses on arsenopyrite. A) Grain from the Nerrin Nerrin prospect showing primary concentric crystallographic zoning. B) Multielement signal of line analysis shown in A. Gold, Pb and Bi signals vary in accordance with the crystallographic zones, where compositionally darker zones contain relatively more Au. C) Grain from the New Boddington deposit, showing irregular compositional zoning that abruptly changes across a fracture. D) Multielement signal of line analysis in C. Note the spike as the fracture is crossed and the differences in signals from the altered (points 1-2) and relatively unaltered (points 2, 3) domains. E) Anhedral grain from the Yunndaga deposit showing advanced stages of post-formation alteration with an alteration rim around the grain boundary. Note the less altered (darker) part of the grain has more pits and a large void, which is also associated with alteration. A visible gold grain is located near the grain boundary. F) Multielement signal of grain in E showing erratic but above detection gold signal. Apy = arsenopyrite.

between Au and trace amounts of Pb, Bi, and, to a lesser extent, with Sb (Fig. 7E, F). Collectively, the SEM, EMP, LA-ICP-MS, and EDS data confirm textural observations that indicate a complex hydrothermal alteration history; invisible gold formed within early low-As arsenopyrite and visible gold formed during later-stage hydrothermal alteration related to the formation of alteration rims and As enrichment.

Discussion

Gold-bearing pyrite and arsenopyrite from five orogenic gold deposits and one prospect within the linked Boorara and Bardoc shear systems (Fig. 1C) exhibit similar paragenetic relationships and gold distribution characteristics. Invisible gold occurs within initial growth zones, and visible gold is associated with later-stage fractures and alteration rims on pyrite-arsenopyrite grains. This is typical of many other pyrite- and arsenopyrite-dominated orogenic ores (e.g., Mumin et al., 1994; Oberthür et al., 1997; Genkin et al., 1998). Backscattered electron images (Figs. 2D, 5C, and 8A, B) further illustrate that late-stage visible gold is associated with chemically modified zones within pyrite and arsenopyrite.

Broadly similar features have been observed in sediment-hosted disseminated (Carlin style) pyrite ores (Arehart et al., 1993; Palenik et al., 2004), within pyrite from an epithermal Ag-Au deposit (Griffin et al., 1991), within arsenopyrite from the Boliden volcanogenic massive sulfide deposit in Sweden (Wagner et al., 2007), in the Campbell mine, Ontario, Canada (Tarnocai et al., 1997), and within pyrite from the Gressli Zn-Cu deposit in Norway (Craig et al., 1998). Arehart et al. (1993) speculated that temperature decrease, reduction, pH change or decrease in the activity of H_2S could drive As and Au enrichment in pyrite, and possibly also arsenopyrite, whereas Palenik et al. (2004) reported that Au^o particles in As-rich pyrite overgrowths either could be primary or secondary in origin. Griffin et al. (1991) interpreted pyrite overgrowths in an epithermal system to be a product of changes in pH and activity of S within the hydrothermal fluids, driven by rapid pressure fluctuations due to cyclic boiling, or even chaotic submicroscopic variations in fluid composition within the epithermal environment.

A characteristic feature of alteration rims, as determined through quantitative and qualitative LA-ICP-MS analyses, is the trace element variations. In the sample from Golden Ridge (Fig. 2; Table 2), the most striking difference between unaltered and altered pyrite is that select trace elements (Sb, Bi, Ba, Te, Pb, and Sn) are depleted within altered pyrite, and the unaltered parts of the pyrite grains have a more uniform trace element distribution than adjacent alteration rims (Fig. 2E). Arsenopyrite shows more complex variations. Unaltered crystallographic zones in stage 2 arsenopyrite contain variable Au, Pb, Bi, and, to a lesser extent, Co (Fig. 7A, B). In comparison to stage 3 altered rims, unaltered stage 2 arsenopyrite contains more Au and Co and less Mo, Bi, and Sb (Fig. 7C-F). Thus, hydrothermal alteration of pyrite and arsenopyrite not only affects the distribution of Au but also depletes or enriches other trace elements within the sulfide grains.

Gold remobilization

The deposition of invisible gold, followed by the later formation of visible gold, is schematically portrayed in Figure 8.
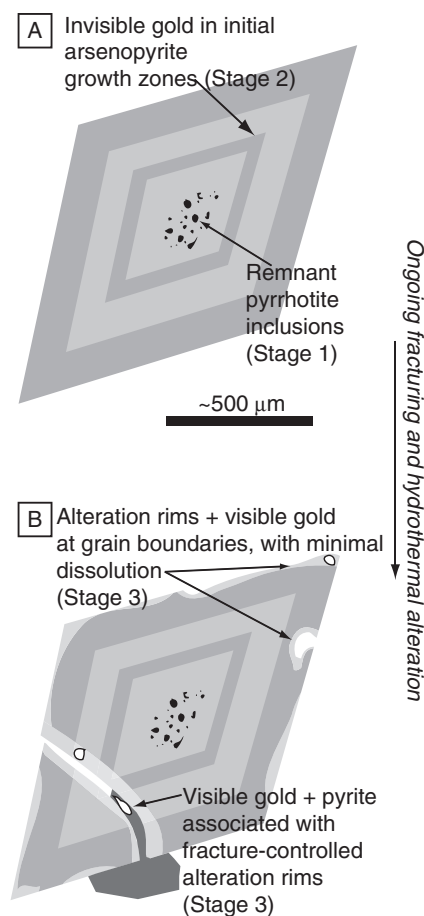

FIG. 8. Schematic representation of the multistage evolution of arsenopyrite, pyrite, and Au. A) The initial growth stage of arsenopyrite (after pyrrhotite) with concentric crystallographic zones that control the distribution of invisible gold. B) Fracturing and continued hydrothermal alteration responsible for the formation of alteration rims and visible gold. Compare with Mumin et al. (1994).

Given that initial pyrite and arsenopyrite grains are characterized by uniform invisible gold distributions (Figs. 2, 7), and that alteration rims (which replaced initial growth phases and are not overgrowths sensu stricto) are depleted in invisible gold, it appears that early invisible gold exsolved and was then remobilized to form at least part of the later-stage visible gold (cf. Mumin et al., 1994; Laroque et al., 1995). The formation of visible gold by hydrothermal alteration of arsenopyrite may provide insights into the formation of orogenic deposits, although the influx of gold during later alteration cannot be discounted. Similar textures are observed in the amphibolite- to granulite-hosted Mt. York, Griffin's Find, and Challenger gold deposits in Australia (Neumayr et al., 1993; Tomkins and Mavrogenes, 2001, 2002), where visible gold was developed at metamorphic growth fronts where arsenopyrite replaced löellingite containing invisible gold.

Stable sulfur isotope and mineralogical data suggest that hydrothermal conditions leading up to and during all stages of gold mineralization were uniformly reduced (Morey et al., 2007b). Overall, reduced conditions are further supported by the ore assemblages for mafic-hosted deposits within the Bardoc tectonic zone (Table 1; Fig. 4), as no minerals indicative

of oxidizing hydrothermal conditions (e.g., hematite, sulfates) were observed. Therefore, the alteration of arsenopyrite and formation of visible gold did not occur through oxidation of the preexisting arsenopyrite and gold species. Various authors (Wagner et al., 1986; Cathelineau et al., 1989; Aylemore and Graham, 1992) have suggested that the solubility of gold in arsenopyrite decreases with increasing temperature, because gold is exsolved from the matrix of arsenopyrite upon heating, forming native gold. This reduction in gold solubility is consistent with the observations of Wagner et al. (2007). These researchers found that in the metamorphosed Boliden VMS deposit, early-formed fine-grained arsenopyrite contains high concentrations of invisible gold, whereas coarse-grained recrystallized and remobilized arsenopyrite, formed near peak

metamorphism (~400°–450°C, 5 kbars; Wagner and Jonsson, 2001), contains significantly less invisible gold. Similarly, Tomkins and Mavrogenes (2001) showed, through LA-ICP-MS analysis, that high temperature arsenopyrite, formed through retrograde metamorphism of invisible gold-bearing löllingite under amphibolite facies experimental conditions, contains low concentrations of invisible gold. It is unknown whether an increase in sulfur fugacity (f_{S_2}) alone can cause exsolution of invisible gold from arsenopyrite.

Hydrothermal alteration of arsenopyrite

The conditions of arsenopyrite alteration can be determined from phase relationships (Clark, 1960; Barton, 1969; Kretschmar and Scott, 1976; Sharp et al., 1985). For Figure 9

FIG. 9. Stability, chemistry, and phase relationships of arsenopyrite. The average compositions of unaltered and altered arsenopyrite (Tables 4, 5) are plotted. Note the temperature change required to fulfill textural and geochemical observations. Phase diagram based on Barton (1969), Kretschmar and Scott (1976) and Sharp et al. (1985). Apy = arsenopyrite, Lö = löellingite, Py = pyrite.

to be used as a thermometer, equilibrium conditions between sulfides and sulfarsenides must have been attained, and diffusional reequilibration must not have taken place. The observation that the oscillatory zoning in arsenopyrite, associated with the initial mineralization event, is preserved indicates that diffusional reequilibration has not affected these domains. Further, the low variability within each deposit of the As and S contents of the arsenopyrite rims suggests that these were in equilibrium with the overprinting hydrothermal event. A paragenetic sequence related to the deposition of invisible and visible gold can be established for all samples studied: pyrrhotite (as inclusions within arsenopyrite) + unaltered arsenopyrite (containing invisible gold) → altered arsenopyrite (arsenic enriched) + pyrite ± pyrrhotite + visible gold.

In Figure 9, the average arsenic contents of unaltered and altered arsenopyrite are plotted. An overall increase in temperature and sulfur fugacity (f_{S_2}) is required for the transition from arsenopyrite + pyrrhotite to arsenopyrite + pyrite ± pyrrhotite. The required temperature increase is on the order of 75° to 100°C, and the increase in f_{S_2} may have been up to 6 orders of magnitude (Fig. 9). These relationships are consistent with the observed gold-arsenopyrite textures and the notion that the solubility of gold in arsenopyrite decreases with increasing temperature. The observed gold-arsenopyrite relationships are best explained by two distinctly separate arsenopyrite-forming events (stage 2 and stage 3 textures), rather than a continuously evolving hydrothermal system, which might be expected to instead preserve gradual changes in mineral chemistry. Furthermore, the higher-temperature event responsible for the pyrite-arsenopyrite rims may have involved only low fluid influx; complete alteration of the arsenopyrite grains is more likely during a pervasive high fluid flux event.

The magnitude of the increase in f_{S_2} can also be assessed through the enrichment of As and a depletion of S within the arsenopyrite grains (Tables 4, 5, Fig. 6; Cathelineau et al., 1989; Cabri et al., 2000):

$$As_xFeS_{y(s)} + zAs_{(aq)} \rightarrow As_{x+z}FeS_{y-z(s)} + zS^{2-}_{(aq)} \quad (1)$$
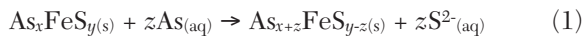
The excess S produced by the formation of alteration rims would also increase the amount of S within the hydrothermal phase and thus raise f_{S_2} (Fig. 9). This is consistent with f_{O_2} versus $a_{\Sigma S}$ phase relationships typical of subamphibolite facies orogenic systems (Fig. 10A; Mikucki and Ridley, 1993). The lack of major arsenopyrite dissolution suggests that f_{O_2} changes likely played a minimal role during arsenopyrite alteration (Heinrich and Eadington, 1986).

The combined effects of temperature and S activity on gold solubility within the hydrothermal fluid are also assessed in Figure 10B. Phase relationships and the alteration path interpreted from Figure 9 suggest that the stage 3 hydrothermal fluid had a significantly greater capacity to carry gold in solution (increasing from ~10^1 to 10^4 ppb Au: Fig. 10B). If this secondary hot, S-rich fluid was significantly undersaturated in gold, it would have removed invisible gold as it replaced the arsenopyrite. However, since abundant visible gold is observed to have formed during this stage, this secondary fluid was likely close to saturation and also could have deposited new metal.
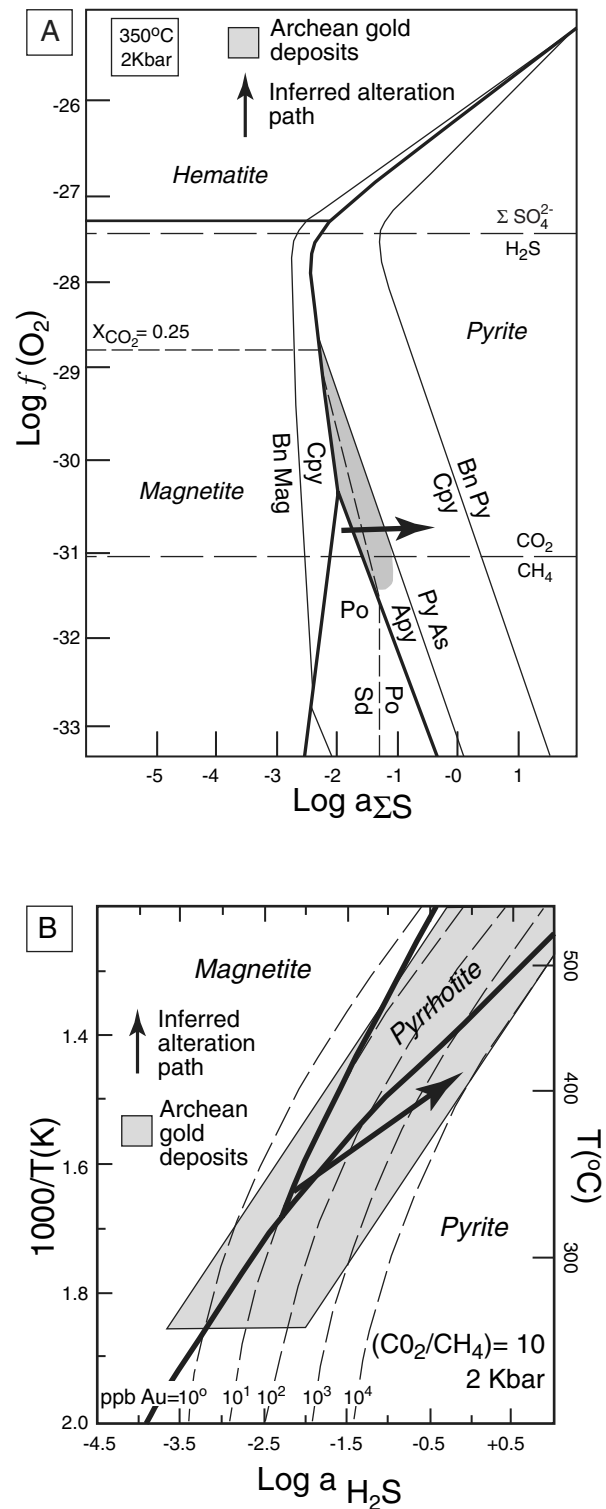
FIG. 10. A) f_{O_2} versus Log $a_{\Sigma S}$ phase stability diagram for subamphibolite facies orogenic gold systems. Shaded area indicates the field representative of most orogenic gold deposits. Arrow indicates the hydrothermal transition as dictated by interpretations made in this study. Redrawn from Mikucki and Roberts (2004). B) Stability diagram showing the effect of Au solubility on temperature and Log a_{H_2S}. Redrawn from Mikucki (1998). Apy = arsenopyrite, Bn = bornite, Cpy = chalcopyrite, Mag = magnetite, Po = pyrrhotite, Py = pyrite, Sd = siderite.

As vein and alteration assemblages are synchronous with deformation (Morey et al., 2007a), the increase in temperature could be an indication that initial arsenopyrite was deposited prior to peak metamorphism. In this scenario, the bulk of the gold would have been deposited invisibly within oscillatory-zoned arsenopyrite under high fluid-flux conditions. Subsequent peak metamorphism would have involved low fluid influx, affecting only the pyrite-arsenopyrite rims, allowing formation of visible gold, possibly via new deposition but largely through exsolution of invisible gold.

However, the dominant alteration mineralogy, which includes chlorite ± biotite (Morey et al., 2007b), is consistent with synpeak metamorphic fluid infiltration, as biotite would not be stable at conditions significantly below peak metamorphism. Furthermore, in one sample described by Morey et al. (2007b), chlorite was interpreted to have replaced biotite, suggesting that some alteration may have been postpeak metamorphic in timing. Thus, it is possible that mineralization occurred during or after regional peak metamorphism. This second scenario is consistent with the prevailing interpretation for orogenic gold deposits regionally in the Yilgarn Block (e.g., Groves et al., 1998), whereby orogenic thickening coupled with erosional denudation causes source regions at depth to undergo prograde metamorphism and devolatilization while midcrustal levels are at peak metamorphism or starting to cool down (cf. Stüwe, 1998). Pyrite devolatilization at depth (i.e., in the source) generates higher proportions of sulfur in the fluid as the temperature increases (Connolly and Cesare, 1993), so as the deeper crust dehydrates over time, escaping fluids should become hotter and more S rich. This increasing fluid temperature and f_{S_2} is consistent with the observed alteration of arsenopyrite. We thus suggest that the observed textures and interpreted f_{S_2} and temperature increase from stage 2 to stage 3 most likely reflect a two-stage evolution, rather than a difference in metamorphic grade, and that mineralization probably occurred during and/or slightly after peak metamorphism.

Conclusions

Pyrite- and arsenopyrite-dominated ore assemblages from the Boorara and Bardoc shear systems (Fig. 1C) share an association with structurally controlled vein systems, similar alteration mineralogy, and the presence of both invisible and visible gold. Invisible gold occurs within unaltered pyrite and arsenopyrite domains, and visible gold is associated with a later-stage alteration event that produced chemically modified alteration rims on these minerals. These alteration rims preferentially formed along the margins of fractures and grain boundaries within pyrite and arsenopyrite. Solid solution behavior and phase stability relationships for arsenopyrite suggest that the later-stage alteration event was driven by an increase in temperature (T) and f_{S_2}, whereas f_{O_2} variations were likely less significant. Alteration rims within pyrite and arsenopyrite are slightly enriched in As and depleted in S, with systematic variations in selected trace elements (Au, Ag, Sb, Ni, Co, Bi, Ba, Pb, Te, Sn, Mo). Apparent prograde metamorphic coronae are observed on arsenopyrite grains, but we suggest that it is more likely that these textures reflect variations in syn- and/or postpeak metamorphic fluid conditions and chemistry at the site of gold deposition.

REFERENCES

Arehart, G.B., Chryssoulis, S.L., and Kesler, S.E., 1993, Gold and arsenic in iron sulfides from sediment-hosted disseminated gold deposits: Implications for depositional processes: ECONOMIC GEOLOGY, v. 88, p. 171–185.

Ashley, P.M., Creagh, C.J., and Ryan, C.G., 2000, Invisible gold in ore and mineral concentrates from the Hillgrove gold-antimony deposits, NSW, Australia: Mineralium Deposita, v. 35, p. 285–301.

Aylmore, M.G., and Graham, J., 1992, Arsenopyrite as a host for refractory gold [abs.], in Griffin, B.J., Johnson, A.W.S., Kuo, J., and Lincoln, F.J., eds., The 1992 Joint Conference on Electron Microscopy and Cell Biology: Electron Microscopy in Mining, Exploration and Metallurgy: Perth, Australia, University of Western Australia, February 10–14, 1992, Proceedings ACEM-12 and ANZSCB-1, p. 43.

Bakken, B.M., Hochella, M.F., Jr., Marshall, A.F., and Turner, A.M., 1989, High-resolution microscopy of gold in unoxidized ore from the Carlin mine, Nevada: ECONOMIC GEOLOGY, v. 84, p. 171–179.

Barton, P.B., Jr., 1969, Thermochemical study of the system Fe-As-S: Geochimica et Cosmochimica Acta, v. 33, p. 841–857.

Brown, S.M., Fletcher, I.R., Stein, H.J., Snee, L.W., and Groves, D.I., 2002, Geochronological constraints on pre-, syn-, and post-mineralization events at the world-class Cleo deposit, Eastern Goldfields Province, Western Australia: ECONOMIC GEOLOGY, v. 97, p. 541–559.

Cabri, L.J., Chryssoulis, S.L., de Villiers, J.P.R., Laflamme, J.H.G., and Buseck, P.R., 1989, The nature of "invisible" gold in arsenopyrite: The Canadian Mineralogist, v. 27, p. 353–362.

Cabri, L.J., Gasper, O.C., Lastra, R., and McMahon, G., 1998, Distribution of gold in tin-rich samples from the Corvo orebody, Portugal: Canadian Mineralogist, v. 36, p. 1347–1360.

Cabri, L.J., Newville, M., Gordon, R.A., Crozier, E.D., Sutton, S.R., McMahon, G., and Jiang, D.T., 2000, Chemical speciation of gold in arsenopyrite: Canadian Mineralogist, v. 38, p. 1265–1281.

Cathelineau, M., Boiron, M.-C., Holliger, P., Marion, P., and Denis, M., 1989, Gold in arsenopyrites; Crystal chemistry, location and state, physical and chemical conditions of deposition: ECONOMIC GEOLOGY MONOGRAPH 6, p. 328–341.

Champion, D.C., and Sheraton, J.W., 1997, Geochemistry and Nd isotope systematics of Archaean granites of the Eastern Goldfields, Yilgarn craton, Australia: Implications for crustal growth processes: Precambrian Research, v. 83, p. 109–132.

Clark, L.A., 1960, The Fe-As-S system: phase relations and applications: ECONOMIC GEOLOGY, v. 55, p. 1345–1381; 1631–1652.

Coleman, L.C., 1957, Mineralogy of the giant Yellowknife gold mine, Yellowknife, N.W.T.: ECONOMIC GEOLOGY, v. 52, p. 400–425.

Connolly, J.A.D., and Cesare, B., 1993, C-O-H-S fluid composition and oxygen fugacity in graphitic metapelites: Journal of Metamorphic Geology, v. 11, p. 379–388.

Craig, J.R., Vokes, F.M., and Solberg, T.N., 1998, Pyrite: Physical and chemical textures: Mineralium Deposita, v. 34, 82–101.

Dahl, N., McNaughton, N.J., and Groves, D.I., 1987, Trace-element and lead isotopic compositions of pyrites as guides to gold and base-metal mineralization: A pilot study: The Minerals and Energy Research Institute of Western Australia Report 22, 57 p.

Danyushevsky, L., Robinson, P., McGoldrick, P., Large, R., and Gilbert, S., 2003 LA-ICPMS of sulphides: Evaluation of an XRF glass disc standard for analysis of different sulphide matrixes: Geochimica et Cosmichimica Acta, v. 67, p. A73-A73.

——2004, Quantitative multi-element analysis of sulphide minerals by laser ablation ICPMS, *in* McPhie, J., and McGoldrick, P., eds., Dynamic Earth: Past, present and future, Geological Society of Australia Abstracts Volume 73, p. 260.

Fleet, M.E., and Mumin, A.H., 1997, Gold-bearing pyrite and arsenopyrite from Carlin Trend gold deposits and laboratory synthesis: American Mineralogist, v. 82, p. 182–193.

Fleet, M.E., MacLean, P.J., and Barbier, J., 1989, Oscillatory-zoned As-bearing pyrite from the strata-bound and stratiform gold deposits: An indicator of ore fluid evolution: ECONOMIC GEOLOGY MONOGRAPH 6, p. 356–362.

Genkin, A.D., Bortnikov, N.S., Cabri, L.J., Wagner, F.E., Stanley, C.J., Safonov, Y.G., McMahon, G., Friedl, J., Kerzin, A.L., and Gamyanin, G.N., 1998, A multidisciplinary study of invisible gold in arsenopyrite from four mesothermal gold deposits in Siberia, Russian Federation: ECONOMIC GEOLOGY, v. 93, p. 463–487.

Griffin, W.L., Ashley, P.M., Ryan, C.G., Soey, S.H., and Suter, G.F., 1991, Pyrite geochemistry in the north arm epithermal As-Au deposit, Queensland, Australia: A proton-microprobe study: Canadian Mineralogist, v. 29, p. 185–198.

Groves, D.I., Phillips, G.N., Ho, S.E., Henderson, C.A., Clark, M.E., and Woad, G.M., 1984, Controls on distribution of Archaean hydrothermal gold deposits in Western Australia, *in* Foster, R. P., ed., Gold '82: The geology, geochemistry and genesis of gold deposits: Rotterdam, Balkema, p. 689–712.

Groves, D. I., Goldfarb, R. J., Gebre-Mariam, M., Hagemann, S. G., and Robert, F., 1998, Orogenic gold deposits: A proposed classification in the context of their crustal distribution and relationship to other gold deposit types: Ore Geology Reviews, v. 13, p. 7–27.

Groves, D.I., Goldfarb, R.J., Knox-Robinson, C.M., Ojala, J., Gardoll, S., Yun, G.Y., and Holyland, P., 2000, Late kinematic timing of orogenic gold deposits and significance for computer-based exploration techniques with emphasis on the Yilgarn Block, Western Australia: Ore Geology Reviews, v. 17, p. 1–38.

Hagemann, S.G., and Cassidy, K.F., 2000, Archean orogenic lode gold deposits: Reviews in Economic Geology, v. 13, p. 9–68.

Heinrich, C.A., and Eadington, P.J., 1986, Thermodynamic predictions of the hydrothermal chemistry of arsenic, and their significance for the paragenetic sequence of some cassiterite-arsenopyrite-base metal sulfide deposits: ECONOMIC GEOLOGY, v. 81, p. 511–529.

Johan, Z., Marcoux, E., and Bonnemaison, M., 1989, Distribution de Au, Sb, As et Fe dans l'arsenopyrite aurifere du Chatelet et de Villeranges (Creuse, Massif Central francais): Les Comptes rendus de l'Académie des sciences, v. 308, p. 293–300.

Kretschmar, U., and Scott, S.D., 1976, Phase relations involving arsenopyrite in the system Fe-As-S and their application: The Canadian Mineralogist, v. 14, p. 364–386.

Lang, J.R., and Baker, T., 2001, Intrusion-related gold systems: The present level of understanding: Mineralium Deposita, v. 36, p. 477–489.

Laroque, A.C.L., Hodgson, C.J., Cabri, L.J., and Jackman, J.A., 1995, Ion-microprobe analysis of pyrite, chalcopyrite and pyrrhotite from the Mobrun VHM deposit in northwestern Quebec: Evidence for metamorphic remobilization of gold: Canadian Mineralogist, v. 33, p. 373–388.

Marsh, E.E., Goldfarb, R.J., Hart, C.J.R., and Johnson, C.A., 2003, Geology and geochemistry of the Clear Creek intrusion-related gold occurrences, Tintina gold province, Yukon, Canada: Canadian Journal of Earth Sciences, p. 681–699.

Mikucki, E.J., 1998, Hydrothermal transport and depositional processes in Archean lode-gold systems: A review: Ore Geology Reviews, v. 13, p. 307–321.

Mikucki, E.J., and Ridley, J.R., 1993, The hydrothermal fluid of Archaean lode-gold deposits at different metamorphic grades: compositional constraints from ore and wallrock alteration assemblages: Mineralium Deposita, v. 28, p. 469–481.

Mikucki, E.J., and Roberts, F.I., 2004, Metamorphic petrography of the Kalgoorlie region, Eastern Goldfields granite-greenstone terrane: METPET database, Geological Survey of Western Australia Record 2003/12, p. 40.

Morey, A.A., Weinberg, R.F., and Bierlein, F.P., 2007a, The structural controls of gold endowment within the Bardoc Tectonic Zone, Eastern Goldfields Province, Western Australia: implications for gold endowment in shear systems: Mineralium Deposita, v. 42, p. 583–600.

Morey, A.A., Weinberg, R.F., Bierlein, F.P., and Davidson, G.J., 2007b, Gold deposits of the Bardoc tectonic zone: A distinct style of orogenic gold in the Archaean Eastern Goldfields Province, Yilgarn craton, Western Australia: Australian Journal of Earth Sciences, v. 54, p. 783–800.

Mumin, A.H., Fleet, M.E., and Chryssoulis, S.L., 1994, Gold mineralization in As-rich mesothermal gold ores of the Bogosu-Prestea mining district of the Ashanti gold belt, Ghana; remobilization of "invisible" gold: Mineralium Deposita, v. 29, p. 445–460.

Neumayr, P., Cabri, L.J., Groves, D.I., Mikucki, E.J., and Jackman, J.A., 1993, The mineralogical distribution of gold and relative timing of gold mineralization in two Archean settings of high metamorphic grade in Australia: Canadian Mineralogist, v. 31, p. 711–725.

Norman, M., Robinson, P., and Clark, D., 2003, Major- and trace-element analysis of sulfide ores by laser-ablation ICP-MS, solution ICP-MS, and XRF: New data on international reference materials: Canadian Mineralogist, v. 41, p. 293–305.

Oberthür, T., Weiser, T., Amanor, J.A., and Chryssoulis, S.L., 1997, Mineralogical siting and distribution of gold in quartz veins and sulphide ores of the Ashanti mine and other deposits in the Ashanti belt of Ghana: Genetic implications: Mineralium Deposita, v. 32, p. 2–15.

Palenik, C.S., Utsunomiya, S., Reich, M., Kesler, S.E., Wang, L., and Ewing, R.C., 2004, "Invisible" gold revealed; direct imaging of gold nanoparticles in a Carlin-type deposit: American Mineralogist, v. 89, p. 1359–1366.

Salier, B.P., Groves, D.I., McNaughton, N.J., and Fletcher, I.R., 2005, Geochronological and stable isotope evidence for widespread orogenic gold mineralization from a deep-seated fluid source at ca. 2.65 Ga in the Laverton Gold Province, Western Australia: ECONOMIC GEOLOGY, v. 100, p. 1363–1388.

Sharp, Z. D., Essene, E. J., and Kelly, W.C., 1985, A re-examination of the arsenopyrite geothermometer: Pressure considerations and applications to natural assemblages: Canadian Mineralogist, v. 23, p. 517–534.

Simon, G., Huang, H., Penner-Hahn, J.E., Kesler, S.E., and Kao, L., 1999, Oxidation state of gold and arsenic in gold-bearing arsenian pyrite: American Mineralogist, v. 84, p. 1071–1079.

Stüwe, K., 1998, Tectonic controls on the timing relationships of metamorphism, fluid production and gold-bearing quartz vein emplacement: Ore Geology Reviews, v. 13, p. 219–228.

Swager, C.P., 1997, Tectono-stratigraphy of late Archaean greenstone terranes in the southern Eastern Goldfields, Western Australia: Precambrian Research, v. 83, p. 11–42.

Swager, C.P., and Griffin, T.J., 1990, Geology of the Archaean Kalgoorlie terrane, northern and southern sheets: Perth, Geological Survey of Western Australia, scale 1:250,000.

Sylvester, P.J., Cabri, L.J., Tubrett, M.N., McMahon, G., Laflamme, J.H.G., and Peregoedova, A., 2005, Synthesis and evaluation of a fused pyrrhotite standard reference material for platinum group element and gold analysis by laser ablation-ICPMS, *in* Törmänen, T.O., and Alapieti, T.T., eds., 10th International Platinum Symposium: Oulu, Geological Survey of Finland, Extended Abstracts, p. 16–20.

Tarnocai, C.A., Hattori, K., and Cabri, L.J., 1997, "Invisible" gold in sulfides from the Campbell mine, Red Lake greenstone belt, Ontario: Evidence for mineralization during the peak of metamorphism: Canadian Mineralogist, v. 35, p. 805–815.

Tomkins, A.G., and Mavrogenes, J.A., 2001, Redistribution of gold within arsenopyrite and löllingite during pro- and retrograde metamorphism: Application to timing of mineralization: ECONOMIC GEOLOGY, v. 96, p. 525–534.

——2002, Mobilization of gold as a polymetallic melt during pelite anatexis at the Challenger gold deposit, South Australia: A metamorphosed Archean deposit: ECONOMIC GEOLOGY, v. 97, p. 1249–1271.

Wagner, F.E., Marion, P.H., and Regnard, J.R., 1986, Mossbauer study of the chemical state of gold in gold ores: Gold 100: South African Institute of Mining and Metallurgy International Conference on Gold, Proceedings, v. 2, p. 435–443.

Wagner, T., and Jonsson, E., 2001, Mineralogy of sulfosalt-rich vein-type ores, Boliden massive sulfide deposit, Skellefte district, northern Sweden: Canadian Mineralogist, v. 39, p. 855–872.

Wagner, T., Klemd, R., Wenzel, T., and Mattsson, B., 2007, Gold upgrading in metamorphosed massive sulfi de ore deposits: Direct evidence from laser-ablation-inductively coupled plasma-mass spectrometry analysis of invisible gold: Geology, v. 35, p. 775–778.

Witt, W.K., 1993, Lithological and structural controls on gold mineralisation in the Archean Menzies-Kambalda area, Western Australia, Australian Journal of Earth Sciences, v. 40, p. 65–86.

Wu, X., and Delbove, F., 1989, Hydrothermal synthesis of gold-bearing arsenopyrite: ECONOMIC GEOLOGY, v. 84, p. 2029–2032.